



Numerical study of nonlinear mixed convection inside stagnation-point flow over surface-reactive cylinder embedded in porous media

Kun Hong¹ · Rasool Alizadeh² · Mostafa Valizadeh Ardalan³ · Amireh Nourbakhsh⁴ · Nader Karimi⁵ · Yang Yang⁶ · Qingang Xiong^{1,7}

Received: 17 December 2019 / Accepted: 28 December 2019 / Published online: 13 January 2020
© Akadémiai Kiadó, Budapest, Hungary 2020

Abstract

Nonlinear mixed convection of heat and mass in a stagnation-point flow of an impinging jet over a solid cylinder embedded in a porous medium is investigated by applying a similarity technique. The problem involves a heterogenous chemical reaction on the surface of the cylinder and nonlinear heat generation in the porous solid. The conducted analysis considers combined heat and mass transfer through inclusions of Soret and Dufour effects and predicts the velocity, temperature and concentration fields as well as the average Nusselt and Sherwood number. It is found that intensification of the nonlinear convection results in development of higher axial velocities over the cylinder and reduces the thickness of thermal and concentration boundary layers. Hence, consideration of nonlinear convection can lead to prediction of higher Nusselt and Sherwood numbers. Further, the investigation reveals that the porous system deviates from local thermal equilibrium at higher Reynolds numbers and mixed convection parameter.

Keywords Nonlinear mixed convection · Stagnation-point flow · Local thermal non-equilibrium · Nonlinear heat generation · Soret effect · Dufour effect

List of symbols

a Cylinder radius (m)
 a_{sf} Interfacial surface area per unit volume of the porous medium (m^{-1})

✉ Qingang Xiong
qgxiong@hyit.edu.cn; qgxiong@126.com

¹ National and Local Joint Engineering Research Center for Mineral Salt Deep Utilization, Key Laboratory for Palygorskite Science and Applied Technology of Jiangsu Province, Huaiyin Institute of Technology, Huai'an 223003, China

² Department of Mechanical Engineering, Quchan Branch, Islamic Azad University, Quchan, Iran

³ Department of Mechanical Engineering, Shahrood University of Technology, Shahrood, Iran

⁴ Department of Mechanical Engineering, Bu-Ali Sina University, Hamedan, Iran

⁵ School of Engineering, University of Glasgow, Glasgow G12 8QQ, UK

⁶ Stanley Black & Decker, Inc., Towson, MD 21286, USA

⁷ IT Innovation Center, General Motors, Warren, MI 48092, USA

Bi Biot number $Bi = \frac{h_{sf} a_{sf} a}{4k_f}$
 C Fluid concentration ($kg\ m^{-3}$)
 C_p Specific heat at constant pressure ($J\ K^{-1}\ kg^{-1}$)
 C_s Concentration ($kg\ m^{-3}$)
 D Molecular diffusion coefficient ($m^2\ s^{-1}$)
 Df Dufour number $Df = \frac{D \cdot k_f}{C_s \cdot C_p} \frac{C_\infty}{(T_w - T_\infty)v}$
 $f(\eta)$ Function related to u-component of velocity
 $f'(\eta)$ Normalised velocity related to w component
 h Heat transfer coefficient ($W\ K^{-1}\ m^{-2}$)
 h_{sf} Interstitial heat transfer coefficient ($W\ K^{-1}\ m^{-2}$)
 k Thermal conductivity ($W\ K^{-1}\ m^{-2}$)
 \bar{k} Freestream strain rate (s^{-1})
 k_1 Permeability of the porous medium (m^2)
 k_m Mass transfer coefficient ($m\ s^{-1}$)
 k_R Kinetic constant ($kg\ m^{-2}\ s^{-1}$)
 k_T Thermal diffusion ratio
 N^* Ratio of concentration to thermal buoyancy forces
 $N^* = \frac{\beta_3 \cdot C_\infty}{\beta_1 (T_w - T_\infty)}$
 Nu Nusselt number
 Nu_m Nusselt number averaged over the surface of the cylinder
 p Pressure (Pa)

P	Dimensionless fluid pressure
P_0	The initial pressure (Pa)
Pr	Prandtl number
Q_h	Heat source parameter $Q_h = \frac{Q_1 a^2}{4k_f}$
q_m	Mass flow at the wall ($\text{kg m}^{-2} \text{s}^{-1}$)
q_w	Heat flow at the wall (W m^{-2})
r	Radial coordinate
Re	Freestream Reynolds number $\text{Re} = \frac{\bar{k} \cdot a^2}{2\nu}$
Sc	Schmidt number $\text{Sc} = \frac{\nu}{D}$
Sr	Soret number $\text{Sr} = \frac{D \cdot k_f \rho (T_w - T_\infty)}{T_\infty C_\infty \alpha}$
Sh	Sherwood number
Sh_m	Average Sherwood number
T_m	Mean fluid temperature (K)
u, w	Velocity components along $(r - \varphi - z)$ -axis (m s^{-1})
z	Axial coordinate

Greek symbols

α	Thermal diffusivity ($\text{m}^2 \text{s}^{-1}$)
β_C	Nonlinear mixed convection parameter for concentration $\beta_C = \frac{\beta_4 \cdot C_\infty}{\beta_3}$
β_t	Nonlinear mixed convection parameter for temperature $\beta_t = \frac{\beta_2 (T_w - T_\infty)}{\beta_1}$
γ	Modified conductivity ratio $\gamma = \frac{k_f}{k_s}$
γ^*	Damköhler number $\gamma^* = \frac{k_R \cdot a}{2D} \frac{1}{C_\infty}$
η	Similarity variable, $\eta = \left(\frac{r}{a}\right)^2 C_\infty$
$\theta(\eta)$	Non-dimensional temperature
λ	Permeability parameter, $\lambda = \frac{a^2}{4k_1}$
ε	Porosity
Λ	Dimensionless temperature difference $\Lambda = \frac{(T_w - T_\infty)}{T_\infty}$
μ	Dynamic viscosity of fluid (N s m^{-2})
ν	Kinematic viscosity of the fluid ($\text{m}^2 \text{s}^{-1}$)
ρ	Density of fluid (kg m^{-3})
ϕ	Dimensionless concentration
φ	Angular (circumferential) coordinate

Subscripts

w	Condition on the surface of the cylinder
∞	Far field
f	Fluid
s	Solid

Introduction

The problem of impinging flow over a porous foam has received a sustained attention in engineering literature [1–4]. This is due to the wide application of this flow configuration in heat sinks [5] and chemical reactors [6]. In particular, the use of stagnation-point flows over surfaces covered by a porous medium is common in catalytic chemical reactors [7,

8]. Since temperature and concentration of species have pronounced effects upon the performance of catalytic reactors, accurate prediction of these quantities is of primary importance in reactor design. For heterogenous catalysts covered by porous inserts, this requires precise analysis of transport phenomena in the porous medium through considering the combined modes of heat and mass transfer.

The basic problem of convective heat transfer in a porous foam placed on a flat solid surface and subject to an impinging flow has been studied extensively, e.g. [9–11]. For conciseness reasons, here, those studies are not reviewed, and the reader is referred to the previous works of the authors for comprehensive reviews of the literature [12–14]. It is, nonetheless, emphasised that most previous investigations of stagnation-point flow through porous media assumed local thermal equilibrium in porous media, see, for example, [15–17]. This assumption although offering a mathematical convenience can jeopardise the accuracy of analysis in porous media that include chemical reactions [18, 19]. Therefore, the less restrictive assumption of local thermal non-equilibrium should be in place, instead. This requires addition of two energy equations for the solid and fluid phases of the porous medium and thus makes the problem mathematically involved. Such analysis was conducted by Jang and Tzeng [20], who considered impinging cooling of porous metallic foam heat sink under local thermal non-equilibrium. These authors found that implementation of a highly porous foam can boost the heat transfer from the flat plate by a factor of two or three [20]. In a subsequent work, the same group of authors repeated the analysis experimentally and confirmed their numerical findings [21]. Later, Wong and Saeid [22] advanced this heat transfer study through inclusion of buoyancy effects and considering mixed convection in their numerical investigation. They conducted an extensive parametric study and showed that thermal conductivity ratio and Biot number in the porous medium are the key parameters for maintaining the system under local thermal equilibrium [22]. The results of Wong and Saeid further indicated that increasing the porosity of the metal foam can lead to higher values of Nusselt number. Later, Wong used a similar numerical setting in an experimental and numerical study of impinging flow on a porous block and demonstrated an overall similarity between the experimentally recorded and computationally predicted temperature fields [23]. The same problem under turbulent flow regime was investigated numerically by Hwang and Yang [24], who reported that the qualitative trends in heat transfer behaviour of the system are similar to that under laminar flow.

Currently, there exist several studies on mixed convection in stagnation-point flow in porous media. Marafie et al. [25] conducted a numerical work on this problem by applying a finite element technique. In keeping with Jang and Tzeng

[20], Marafie et al. [25] showed that addition of the impinging flow enhances the rate of heat transfer by more than two times. These authors showed that there is a critical height of the porous block. Thickening the porous block prior to reaching the critical height results in increasing the Nusselt number. However, further thickening of the block beyond the critical thickness leads to reduction of Nusselt number [25]. Harris et al. [26] presented a similarity analysis of the boundary layer flows at the stagnation-point upon a porous block located vertically. A computational study about mixed convection in jet flows over a porous insert showed that increases in Reynolds number and jet width render higher values of the mean Nusselt number [27]. It was further demonstrated that Nusselt number is enhanced by reducing the gap between the impinging flow and the heated part [27].

In the work of Kokubun and Fachini [3], an analytical solution was presented for the impinging flows over an infinitely long, horizontally positioned porous plate, experiencing different types of thermal boundary conditions. This investigation revealed that a dimensionless parameter, involving information about the transfer characteristics of the fluid and porous solid, governs the process of heat transfer. A numerical and experimental study was conducted by Feng et al. [5] on the problem of stagnation-point flow over a heated porous plate. They investigated a metal porous medium and a finned metal foam and showed that increases in the metal foam thickness reduce the heat transfer coefficient. However, such trend was not observed for the metal finned foam [5]. In a relatively recent study, Buonomo et al. [28] analysed the heat transfer process as a laminar jet vertically interacts with a horizontal, confined porous plate in an axisymmetric setting. Buonomo et al. [28] showed that Peclet number dominates the assisting and opposing configurations of free and forced convection. Makinde [29] and Rosca and Pop [30] examined mixed convection in stagnation-point flows impinging on a vertical porous plate. Magnetic effects and radiation of heat were also included in the analysis of mixed convection inside vertical, porous inserts [31]. An important common point in almost all studies on mixed convection in porous media is consideration of flat porous plates, and thus, curved porous configurations have been rarely investigated.

Nonlinear convection was included in a recent numerical work by Qayyum et al. [32], who analysed the nonlinear convection of a nanofluid over a heated stretching surface. Nonlinearity was included in the problem by considering nonlinear temperature and concentration terms in the form of $(T - T_\infty)^2$ and $(C - C_\infty)^2$ in the buoyancy term of momentum equation. Similar studies were conducted by Qayyum et al. [33] and Hayat et al. [34], who further included a heat source that was linearly dependent upon the fluid temperature. It is essential to note that the works of Qayyum et al. [32, 33] and Hayat et al. [34] were not concerned with flows

inside porous media. Other recent investigations of nonlinear convection in boundary layer flows include those of Hayat et al. [35] and Khan et al. [36]. It appears that currently there is no study on nonlinear convection in porous media.

The present study aims to fill the gaps identified in the preceding review of the literature. Towards this goal, nonlinear mixed convection of heat and mass in a stagnation-point flow developed over a cylinder embedded in porous media is investigated numerically. To establish a direct connection to catalytic chemical reactors, it is assumed that a simple surface reaction takes place at the external surface of the cylinder.

Theoretical and numerical methods

Configuration of the problem, governing equations and assumptions

A schematic of the problem under investigation is shown in Fig. 1. A cylinder with radius a centred at $r = 0$ has been coated by a catalyst and embedded in a porous medium. Surface temperature on the external wall of the cylinder is maintained constant. The external flow over the cylinder includes an axisymmetric radial stagnation-point flow with the strain rate of \bar{k} . The current analysis considers the following assumptions.

- The fluid flow is under steady-state condition. It is also laminar and incompressible, while the cylinder is infinitely long and features zero permeability.

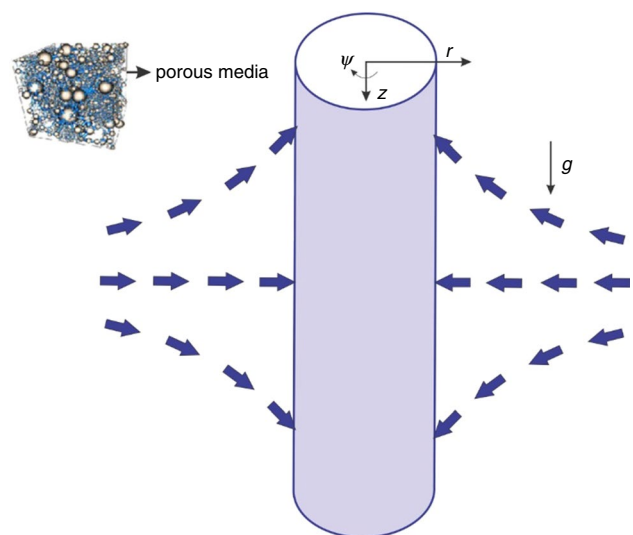


Fig. 1 Schematics of the investigated problem: a vertical cylinder embedded in porous media under radial stagnation flow

- The catalytic reactions on the surface of the cylinder are temperature independent and of zeroth order [37–39].
- Soret and Dufour effects on the transport of heat and mass are taken into account.
- The porous medium around the cylinder is under local thermal non-equilibrium (LTNE) and is also homogenous and isotropic.
- Thermal radiation and frictional dissipation of the flow kinetic energy are ignored. However, gravitational effects and nonlinear convection of heat and mass are considered.
- Density and heat conductivity as well as porosity and specific heat capacities are constant. As a result, the thermal dispersion in the porous medium is negligibly small.
- Pore-scale Reynolds number is moderate, and therefore, Forchheimer term in the model of momentum transfer is ignored.

It is clarified that zeroth-order surface reactions are often used to approximate the kinetics of many catalytic reactions [40]. Hence, they are of practical importance.

Assuming a nonlinear, double-diffusive mixed convection and by employing a cylindrical coordinate, the governing equations and boundary conditions can be written in the following forms.

The conservation of mass is as follows:

$$\frac{\partial u}{\partial r} + \frac{u}{r} + \frac{\partial w}{\partial z} = 0. \tag{1}$$

Momentum transfer in the radial direction is governed by

$$\begin{aligned} \frac{1}{\varepsilon^2} \left(u \frac{\partial u}{\partial r} + w \frac{\partial u}{\partial z} \right) &= -\frac{1}{\rho} \frac{\partial p}{\partial r} \\ &+ \frac{\nu}{\varepsilon} \left(\frac{\partial^2 u}{\partial r^2} + \frac{1}{r} \frac{\partial u}{\partial r} - \frac{u}{r^2} + \frac{1}{r^2} \frac{\partial^2 u}{\partial \varphi^2} + \frac{\partial^2 u}{\partial z^2} \right) - \frac{\nu}{k_1} u, \end{aligned} \tag{2}$$

and that in the axial direction, it is given by [35, 36]

$$\begin{aligned} \frac{1}{\varepsilon^2} \left(u \frac{\partial w}{\partial r} + w \frac{\partial w}{\partial z} \right) &= -\frac{1}{\rho} \frac{\partial p}{\partial z} \\ &+ \frac{\nu}{\varepsilon} \left(\frac{\partial^2 w}{\partial r^2} + \frac{1}{r} \frac{\partial w}{\partial r} + \frac{1}{r^2} \frac{\partial^2 w}{\partial \varphi^2} + \frac{\partial^2 w}{\partial z^2} \right) \\ &\mp g \left[\beta_1 (T_f - T_\infty) + \beta_2 (T_f - T_\infty)^2 \right] \\ &+ g \left[\beta_3 (C - C_\infty) + \beta_4 (C - C_\infty)^2 \right] - \frac{\nu}{k_1} w. \end{aligned} \tag{3}$$

Equation (3) includes the nonlinear terms appearing as body forces on the right-hand side. The transfer of heat in the fluid phase reduces to

$$\begin{aligned} u \frac{\partial T_f}{\partial r} + w \frac{\partial T_f}{\partial z} &= \alpha_f \left(\frac{\partial^2 T_f}{\partial r^2} + \frac{1}{r} \frac{\partial T_f}{\partial r} + \frac{1}{r^2} \frac{\partial^2 T_f}{\partial \varphi^2} + \frac{\partial^2 T_f}{\partial z^2} \right) \\ &+ \frac{h_{sf} \cdot a_{sf}}{\rho \cdot C_p} (T_s - T_f) \\ &+ \frac{Dk_T}{C_s \cdot C_p} \left(\frac{\partial^2 C}{\partial r^2} + \frac{1}{r} \frac{\partial C}{\partial r} + \frac{1}{r^2} \frac{\partial^2 C}{\partial \varphi^2} + \frac{\partial^2 C}{\partial z^2} \right). \end{aligned} \tag{4}$$

The last term on the left-hand side of Eq. (4) denotes Dufour effect [37, 38]. The transfer of heat in the solid phase of the porous medium is expressed by

$$\begin{aligned} k_s \left(\frac{\partial^2 T_s}{\partial r^2} + \frac{1}{r} \frac{\partial T_s}{\partial r} + \frac{1}{r^2} \frac{\partial^2 T_s}{\partial \varphi^2} + \frac{\partial^2 T_s}{\partial z^2} \right) &- h_{sf} \cdot a_{sf} (T_s - T_f) \\ &+ \left[Q_1 (T_s - T_\infty) + Q_2 (T_s - T_\infty)^2 \right] = 0. \end{aligned} \tag{5}$$

The following equation governs the transport of chemical species throughout the porous medium in which the thermal diffusion of mass (Soret effect) has been considered [38, 39]:

$$\begin{aligned} u \frac{\partial C}{\partial r} + w \frac{\partial C}{\partial z} &= D \left(\frac{\partial^2 C}{\partial r^2} + \frac{1}{r} \frac{\partial C}{\partial r} + \frac{1}{r^2} \frac{\partial^2 C}{\partial \varphi^2} + \frac{\partial^2 C}{\partial z^2} \right) \\ &+ \frac{Dk_T}{T_m} \left(\frac{\partial^2 T_f}{\partial r^2} + \frac{1}{r} \frac{\partial T_f}{\partial r} + \frac{1}{r^2} \frac{\partial^2 T_f}{\partial \varphi^2} + \frac{\partial^2 T_f}{\partial z^2} \right). \end{aligned} \tag{6}$$

In Eqs. (4–6), the subscripts “*f*” and “*s*” denote the fluid and solid phase of the porous medium, respectively.

The boundary conditions of momentum equations are given as follows.

$$r = a : w = 0, u = 0, \tag{7}$$

$$r = \infty : w = 2\bar{k}z, u = -\bar{k} \left(r - \frac{a^2}{r} \right), \tag{8}$$

The no-slip condition over the external wall of the cylinder is represented by Eq. (7). Further, Eq. (8) implies that the solution of viscous flow behaves similar to that for Hiemenz flow, the potential flow solution as $r \rightarrow \infty$ [41–43]. This can be verified by starting from the continuity equation in the followings. $-\frac{1}{r} \frac{\partial(ru)}{\partial r} = \frac{\partial w}{\partial z}$ Constant = $2\bar{k}z$, and integrating in r and z directions with boundary conditions, $w = 0$ when $z = 0$ and $u = 0$ when $r = a$.

The boundary conditions for the transport of thermal energy are given by

$$\begin{aligned} r = a : T_f &= T_w = \text{Constant}, \\ T_s &= T_w = \text{Constant}, \end{aligned} \tag{9}$$

$$\begin{aligned} r = \infty : T_f &= T_\infty, \\ T_s &= T_\infty, \end{aligned}$$

where T_w is the temperature of the surface of cylinder and T_∞ is that of the freestream flow.

The boundary condition for mass transfer is given by

$$r = a: \frac{\partial C}{\partial r} = -\frac{k_R}{D} = \text{Constant}, \tag{10}$$

$$r = \infty: C \rightarrow C_\infty$$

where D is the Fickian diffusion coefficient, k_R is the kinetic constant pertinent to a zeroth-order heterogenous reaction [38, 39], and C_∞ denotes the concentration of species in the freestream.

Self-similar analysis

The governing Eqs. (1–6) are reduced by applying the following similarity transformations.

$$u = -\frac{\bar{k} \cdot a}{\sqrt{\eta}} f(\eta), \quad w = [2\bar{k}f'(\eta)]z, \quad p = \rho_f \bar{k}^2 a^2 P, \tag{11}$$

where $\eta = \left(\frac{r}{a}\right)^2$ is the non-dimensional radial variable. Relations (11) satisfy the continuity of mass [Eq. (1)], and substitution into momentum equations [Eqs. (2), (3)] renders the following system of coupled, ordinary differential equations.

$$[\eta f'''' + f'''] + \frac{1}{\varepsilon^2} \text{Re} [1 + ff' - (f')^2] + \lambda [1 - f'] \mp \lambda_1 \theta_f [1 + \beta_1 \cdot \theta_f] + \lambda_1 \cdot N^* \cdot \phi [1 + \beta_C \cdot \phi] = 0, \tag{12}$$

$$P - P_0 = -\frac{1}{2\varepsilon^2} \left(\frac{f^2}{\eta}\right) - \frac{1}{\varepsilon} \left[\left(\frac{f'}{\text{Re}}\right) + \frac{\lambda}{\text{Re}} \int_1^\eta \frac{f}{\eta} d\eta\right] - 2\left[\frac{1}{\varepsilon^2} + \frac{\lambda}{\text{Re}}\right] \left(\frac{z}{a}\right)^2, \tag{13}$$

where $\text{Re} = \frac{\bar{k} \cdot a^2}{2\nu}$ shows the Reynolds number of the freestream, $\lambda = \frac{a^2}{\varepsilon}$ is the permeability parameter, $\lambda_1 = \frac{\text{Gr}}{\text{Re}^2} = \frac{g \cdot \beta_1 (T_w - T_\infty)}{4k_1}$ is the dimensionless mixed convection parameter, $\beta_1 = \frac{4\eta \bar{k}^2 (T_w - T_\infty)}{\beta_1}$ is the nonlinear mixed convection parameter for temperature, $\beta_C = \frac{\beta_4 \cdot C_\infty}{\beta_3}$ denotes the nonlinear mixed convection parameter for concentration, $N^* = \frac{\beta_3 \cdot C_\infty}{\beta_1 (T_w - T_\infty)}$ represents the ratio of concentration to thermal buoyancy forces, and prime represents the differentiation with respect to the radial variable η .

Considering the transport of momentum, the boundary conditions for Eq. (12) reduce to

$$\eta = 1: f'(1) = 0, \quad f(1) = 0, \tag{14}$$

$$\eta \rightarrow \infty: f'(\infty) = 1. \tag{15}$$

The following transformation is introduced [43, 44], to non-dimensionalise the energy equation,

$$\theta_f(\eta) = \frac{T_f(\eta) - T_\infty}{T_w - T_\infty}. \tag{16}$$

By substituting Eqs. (11) and (16) into Eq. (4) and through ignoring the dissipation terms, the following relation is developed

$$\eta \theta_f'' + \theta_f' + \text{Re} \cdot \text{Pr} \cdot (f \cdot \theta_f') + \text{Bi}(\theta_s - \theta_f) + \text{Df} \cdot \text{Pr} [\eta \phi'' + \phi'] = 0, \tag{17}$$

where $\text{Bi} = \frac{h_{st} a_{st} a}{4k_f}$ is the Biot number and $\text{Df} = \frac{D \cdot k_T}{C_s \cdot C_p} \frac{C_\infty}{(T_w - T_\infty)^v}$ is the Dufour number, and the pertinent boundary conditions can be written as:

$$\eta = 1: \theta_f(1) = 1 \tag{18a}$$

$$\eta \rightarrow \infty: \theta_f(\infty) = 0 \tag{18b}$$

Substitution of Eqs. (11) and (16) into Eq. (5) results in

$$\eta \theta_s'' + \theta_s' - \text{Bi} \cdot \gamma (\theta_s - \theta_f) + Q_h \cdot \gamma \cdot \theta_s [1 + \beta_h \cdot \theta_s] = 0, \tag{19}$$

where $\gamma = \frac{k_f}{k_s}$ is the modified conductivity ratio, $Q_h = \frac{Q_1 a^2}{4k_f}$ denotes the heat source parameter, and $\beta_h = \frac{Q_2 (T_w - T_\infty)}{Q_1}$ is the nonlinear heat source parameter, while the boundary conditions are expressed by:

$$\eta = 1: \theta_s(1) = 1 \tag{20a}$$

$$\eta \rightarrow \infty: \theta_s(\infty) = 0 \tag{20b}$$

Transformation (21) is used, to non-dimensionalise the mass transfer Eq. (6),

$$\phi(\eta) = \frac{C(\eta) - C_\infty}{C_\infty}. \tag{21}$$

By substituting Eqs. (14) and (16) into Eq. (6), the following equation is developed

$$\text{Pr} [\eta \phi'' + \phi'] + \text{Sr} \cdot \text{Sc} [\eta \theta_f'' + \theta_f'] + \text{Re} \cdot \text{Pr} \cdot \text{Sc} (f \cdot \phi') = 0 \tag{22}$$

where $\text{Sc} = \frac{\nu}{D}$ is the Schmidt number and $\text{Sr} = \frac{D \cdot k_T}{T_m} \frac{(T_w - T_\infty)}{C_\infty \cdot \alpha}$ is the Soret number, and the boundary conditions are:

$$\eta = 1: \phi'(1) = -\gamma^* \tag{23a}$$

$$\eta \rightarrow \infty: \phi(\infty) = 0 \tag{23b}$$

where $\gamma^* = \frac{k_R \cdot a}{2D} \frac{1}{C_\infty}$ is the Damköhler number. Numerical solutions for Eqs. (12), (17), (19) and (22) along with the boundary conditions (14–15), (18), (20), (23) are developed

Table 1 Verification of grid independency at $Df = 1.0$, $Bi = 0.1$, $Sr = 0.5$, $Re = 5.0$, $\lambda = 10$, $Sc = 0.1$

Mesh size	Nu_m	Sh_m
51×18	1.540873	0.588014
102×36	1.499256	0.555648
204×72	1.479155	0.527381
408×144	1.465920	0.467275
816×288	1.465773	0.468014

by employing an implicit, iterative tri-diagonal finite difference method [45].

Nusselt and Sherwood numbers

The rate of heat transfer for the fluid phase and the local convection coefficient are defined as

$$h = \frac{q_w}{T_w - T_\infty} = \frac{-k_f \left(\frac{\partial T_f}{\partial r} \right)_{r=a}}{T_w - T_\infty} = -\frac{2k_f}{a} \frac{\partial \theta_f(1)}{\partial \eta}, \tag{24}$$

and

$$q_w = -\frac{2k_f}{a} \frac{\partial \theta_f(1)}{\partial \eta} T_w - T_\infty. \tag{25}$$

Thus, Nusselt number calculated on the external surface of the cylinder is expressed by

$$Nu = \frac{h \cdot a}{2k_f} = -\theta'(1). \tag{26}$$

In a similar way, the local rate of mass transfer and mass transfer coefficient are given by

$$k_m = \frac{q_m}{C_w - C_\infty} = \frac{-D \left(\frac{\partial C}{\partial r} \right)_{r=a}}{C_w - C_\infty} = -\frac{2D}{a} \frac{\partial \phi(1)}{\partial \eta}. \tag{27}$$

and

$$q_m = -\frac{2D}{a} \frac{\partial \phi(1)}{\partial \eta} C_w - C_\infty. \tag{28}$$

Table 2 Validation of the numerical method by comparison between the current simulations and those of Wang [36] for large porosity and permeability

η	$Re = 1.0$				$Re = 10$			
	Wang [36]		Current simulations		Wang [36]		Current simulations	
	f	f'	f	f'	f	f'	f	f'
1.2	0.02667	0.25302	0.02693	0.25993	0.06638	0.58982	0.06631	0.06610
1.4	0.09665	0.43724	0.09652	0.43710	0.21400	0.84821	0.21393	0.21379
1.6	0.19836	0.57315	0.19828	0.57329	0.39532	0.94852	0.39541	0.39535
1.8	0.32361	0.67444	0.32365	0.67438	0.58919	0.98380	0.58914	0.58926
2.0	0.46674	0.75054	0.46683	0.75046	0.78731	0.99522	0.78735	0.78729

Therefore, Sherwood number can be written as

$$Sh = \frac{k_m \cdot a}{2D} = -\phi'(1). \tag{29}$$

Grid independency and validation

To ensure achieving numerical results that are grid independent, values of the surface-averaged Nusselt and Sherwood number were computed for grid sizes of 51×18 , 102×36 , 204×72 , 408×144 and 816×288 . As shown in Table 1, there are no considerable changes in the average Nusselt and Sherwood numbers for the (η, φ) mesh sizes of (204×72) , (408×144) and (816×288) . Hence, a (408×144) grid in $\eta - \varphi$ directions was chosen for the computational domain of the current work. To capture the sharp gradients of velocity, temperature and concentration around the external surface of the cylinder, a non-uniform grid was applied in η direction, while a homogeneous mesh was used in the angular direction. In the current work, the computational domain extends to $\varphi_{max} = 360^\circ$ and $\eta_{max} = 15$. It is important to note that η_{max} essentially corresponds to $\eta \rightarrow \infty$. This is because for all cases investigated in this work, η_{max} is located outside the concentration, momentum and thermal boundary layers. It is assumed that when the disparity between the two consecutive iterations becomes less than 10^{-7} , the convergence criterion in the numerical simulations has been met, and thus, the iterative process is stopped. On the basis of the utilised numerical method, the numerical error is deemed to be of $O(\Delta\eta)^2$ [45].

Tables 2 and 3 show that for very large permeability and porosity of one (a clear region) and when the mass transfer and gravitational effects are suppressed, the numerical simulations developed in “Theoretical and numerical methods” section reduce to those of Wang [46] and Gorla [47] for the impinging flow on a circular cylinder. Also, although not shown in this section, it was verified that for large Biot numbers, the current LTNE results become identical to those developed in an earlier work of the authors under LTE condition [12]. This rational trend provides another evidence for correctness of the current simulations.

Table 3 Comparison between the current simulations and those of Gorla [37] for very large porosity and permeability

Re	f		θ	
	Gorla [37]	Current simulations	Gorla [37]	Current simulations
0.01	0.12075	0.12051	0.84549	0.84557
0.1	0.22652	0.22659	0.73715	0.73701
1.0	0.46647	0.46683	0.46070	0.46045
10	0.78731	0.78725	0.02970	0.02983

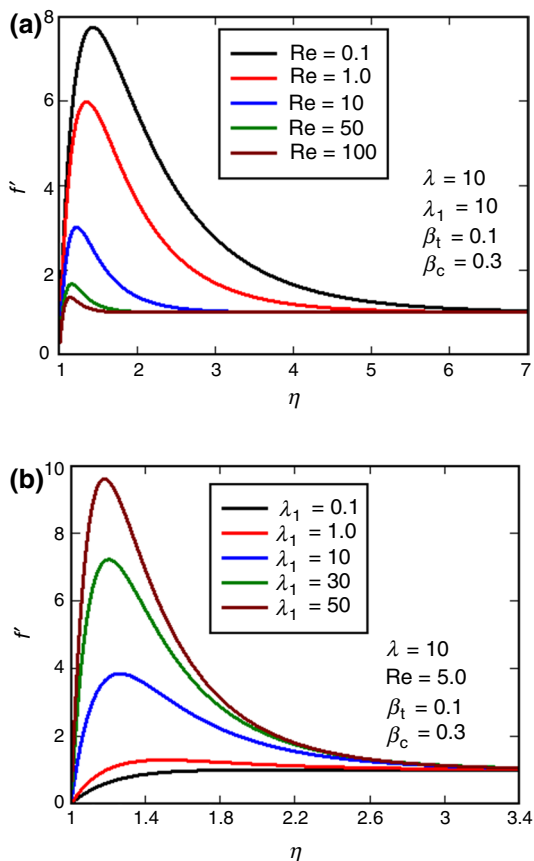


Fig. 2 Variation in velocity related to w component $f'(\eta)$ for varying **a** Reynolds number, **b** dimensionless mixed convection parameter, $Df = 0.1$, $Bi = 0.1$, $Sr = 0.5$, $Re = 5.0$, $Sc = 0.1$, $\lambda = 10$, $\lambda_1 = 10$, $\beta_t = 0.1$, $\beta_c = 0.3$, $\beta_h = 0.1$

Results and discussion

Temperature and concentration fields

Figure 2a depicts the radial distribution of non-dimensionalised axial velocity (f') for different Reynolds numbers. As expected, there is a hydrodynamic boundary layer over the cylinder in which flow velocity features an overshoot.

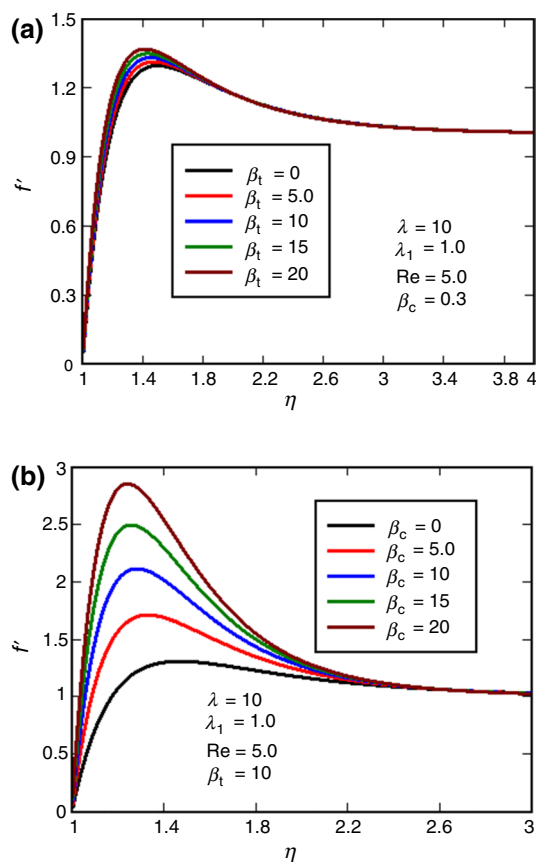


Fig. 3 Variation in velocity related to w component $f'(\eta)$ for different values of **a** nonlinear mixed convection parameter for temperature, **b** nonlinear mixed convection parameter for concentration, $Df = 0.1$, $Bi = 0.1$, $Sr = 0.5$, $Re = 5.0$, $Sc = 0.1$, $\lambda = 10$, $\lambda_1 = 10$, $\beta_t = 0.1$, $\beta_c = 0.3$, $\beta_h = 0.1$

In keeping with the classical behaviours of viscous flows at low Reynolds number, the hydrodynamic boundary layer grows in thickness as Reynolds number decreases. Figure 2a also shows that the amplitude of the overshoot increases for lower values of Reynolds number. The observed overshoot is because of the influence of buoyancy forces upon the fluid velocity, which becomes more noticeable in low-momentum flows. Figure 2b further elaborates on this by showing the radial variation in axial velocity for different mixed convection parameters. At low values of mixed convection parameter, for which the flow approaches forced convection, there is almost no velocity overshoot and a typical profile of forced convection boundary layer is recaptured. However, by increasing the share of natural convection at higher values of mixed convection parameter, the velocity overshoot grows in magnitude. Interestingly, as the numerical value of mixed convection exceeds 10, the thickness of the hydrodynamic boundary layer becomes nearly indifferent to this value. This along with the trend observed in Fig. 2a confirms that the

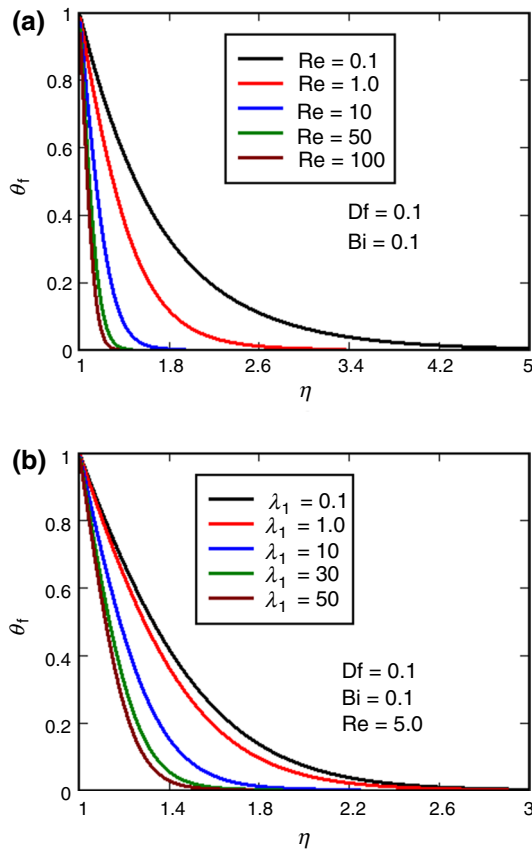


Fig. 4 Variation in dimensionless fluid temperature $\theta_f(\eta)$ for varying **a** Reynolds number, **b** dimensionless mixed convection parameter, $Df = 0.1$, $Bi = 0.1$, $Sr = 0.5$, $Re = 5.0$, $Sc = 0.1$, $\lambda = 10$, $\lambda_1 = 10$, $\beta_t = 0.1$, $\beta_c = 0.3$, $\beta_h = 0.1$

boundary layer thickness in the current problem is dominated by Reynolds number.

Figure 3 shows the effects of nonlinear mixed convection upon the profiles of dimensionless axial velocity. Both parts of this figure indicate that strengthening of nonlinear convection results in higher amplitudes of velocity overshoot in the hydrodynamic boundary layer. Yet, in agreement with that discussed earlier, the boundary layer thickness remains independent of nonlinear mixed convection. This is an important result as it illustrates the influence of nonlinear mixed convection upon the hydrodynamics of the problem. Figure 3b implies that such influences can be significant. Figure 3 clearly shows that the influences of nonlinear mixed convection parameter for concentration (β_c) are stronger than those of nonlinear mixed convection for temperature (β_t). The reason for this difference is not immediately obvious and is most probably due to the strongly nonlinear nature of momentum transport in mixed convection, as reflected by Eq. (12). Unlike conventional mixed convection modelling, the current problem models the buoyancy effects of temperature and concentration difference through strongly nonlinear

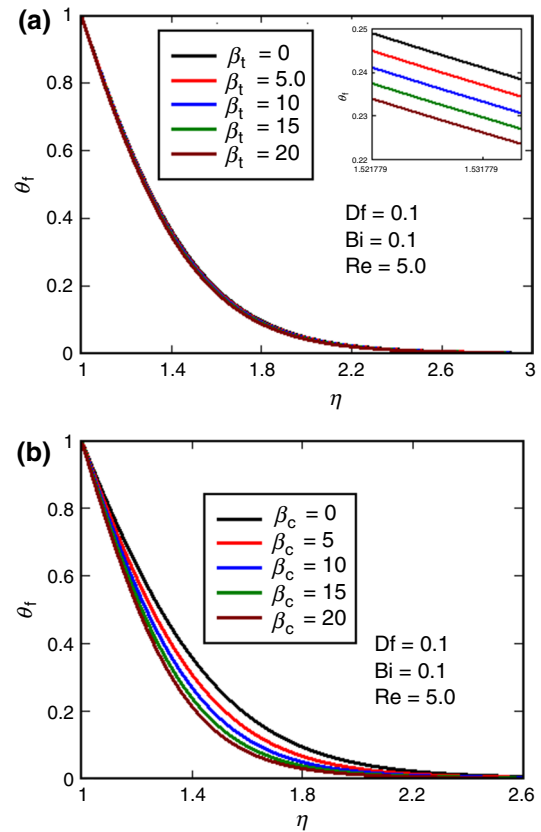


Fig. 5 Variation in dimensionless fluid temperature $\theta_f(\eta)$ for different values of **a** nonlinear mixed convection parameter for temperature, **b** nonlinear mixed convection parameter for concentration, $Df = 0.1$, $Bi = 0.1$, $Sr = 0.5$, $Re = 5.0$, $Sc = 0.1$, $\lambda = 10$, $\lambda_1 = 10$, $\beta_t = 0.1$, $\beta_c = 0.3$, $\beta_h = 0.1$

terms [see Eq. (3)]. This can lead to complex interactions between transport of momentum and those of heat and mass [Eqs. (4), (5), (6)] and imbalance the effects of mixed convection parameters upon momentum transfer.

The effects of Reynolds number and permeability of the porous medium on the dimensionless temperature of the fluid phase are shown in Fig. 4. According to Fig. 4a, at any radial distance from the surface of the cylinder, increases in Reynolds number result in reduction in the dimensionless temperature of the fluid. It should be noted that according to the definition of dimensionless temperature (Eq. 6), lower values of this quantity imply a fluid temperature close to that of the impinging flow and the values of dimensionless temperature close to unity indicate proximity to the wall temperature. Figure 4a shows that at any radius, increases in Reynolds number result in the reduction in fluid temperature. It also shows that the thickness of thermal boundary layer decreases at higher values of Reynolds number. It will be later shown that this trend is associated with an increase in the rate of heat transfer. This is to be expected as, in general, increases in Reynolds number and reduction in the

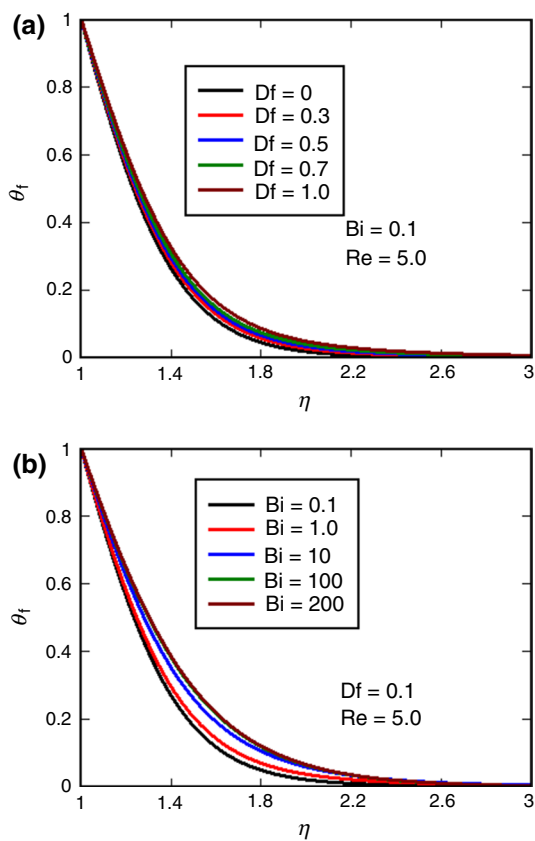


Fig. 6 Variation in dimensionless fluid temperature $\theta_f(\eta)$ for varying **a** Dufour number, **b** Biot number, $Df = 0.1$, $Bi = 0.1$, $Sr = 0.5$, $Re = 5.0$, $Sc = 0.1$, $\lambda = 10$, $\lambda_1 = 10$, $\beta_t = 0.1$, $\beta_c = 0.3$, $\beta_h = 0.1$

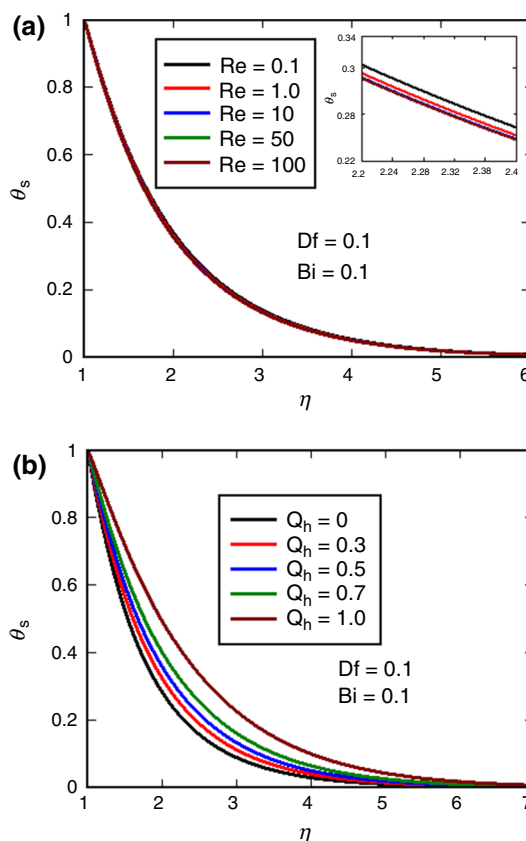


Fig. 7 Variation in dimensionless solid temperature $\theta_s(\eta)$ for varying **a** Reynolds number, **b** heat source parameter, $Df = 0.1$, $Bi = 0.1$, $Sr = 0.5$, $Re = 5.0$, $Sc = 0.1$, $\lambda = 10$, $\lambda_1 = 10$, $\beta_t = 0.1$, $\beta_c = 0.3$, $\beta_h = 0.1$

thickness of thermal boundary layer intensify the convective heat transfer [48]. Figure 4b shows that increases in mixed convection parameter lead to reduction in the dimensionless temperature of the fluid and formation of thinner thermal boundary layer. Hence, convective heat transfer is stronger at higher values of mixed convection parameter. Once again, this is an anticipated result as Reynolds number, and therefore, the strength of forced convection is kept constant in Fig. 4b. Thus, increases in mixed convection strengthen the contribution of natural convection with the heat transfer process.

Figure 5 depicts the effects of β_c and β_T on the dimensionless temperature of the fluid. According to this figure, increases in either of β_c or β_T result in the reduction in dimensionless temperature and lessen the thickness of thermal boundary layer. It follows that the increases in the nonlinear convection parameters intensify the rate of heat transfer. Comparison of Fig. 5a, b shows that the influences of β_c upon the reduction in boundary layer thickness are stronger than those of β_T . This can be attributed to the behaviour observed in Fig. 3 in which variations in β_c affect

the velocity field more significantly in comparison with β_T . Larger velocities induced at higher values of β_c strengthen mixed convection of heat and induce higher rates of heat transfer and smaller thicknesses of the thermal boundary layer. Figure 5b further shows that increases in β_c lead to a slight decrease in the thickness of thermal boundary layer. This implies that by intensifying nonlinear mixed convection, the characteristics of thermal boundary layer approach those of forced convection.

The effects of Dufour and Biot number on the dimensionless temperature of the fluid are shown in Fig. 6. According to this figure, variation in Dufour number leaves modest effects on the fluid temperature. Magnification of Dufour effect slightly increases the dimensionless temperature of fluid and hence renders lower rates of heat transfer. Yet, variation in Biot number appears to feature more pronounced impacts on the fluid temperature. Figure 6a clearly shows that dimensionless fluid temperatures are smaller at lower values of Biot number. This is to be expected, as a low Biot number implies high thermal conductivity of the porous medium, which is a well-known factor in enhancement of heat transfer in porous media [49].

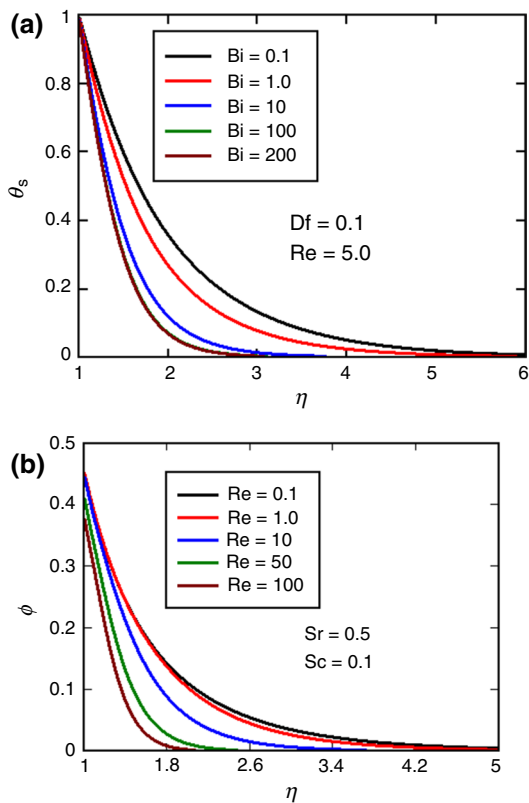


Fig. 8 a Response of dimensionless solid temperature $\theta_s(\eta)$ to changes in the value of Biot number, **b** response of $\phi(\eta)$ for different values of Reynolds number, $Df = 0.1$, $Bi = 0.1$, $Sr = 0.5$, $Re = 5.0$, $Sc = 0.1$, $\lambda = 10$, $\lambda_1 = 10$, $\beta_l = 0.1$, $\beta_c = 0.3$, $\beta_h = 0.1$

Figure 7a shows that changes in Reynolds number have no considerable effect on the dimensionless temperature of the porous solid phase. However, variation in heat source parameter can significantly alter the porous solid temperature (Fig. 7b). As shown in Fig. 8a, Biot number has also a significant effect on the temperature of the porous solid phase. At lower Biot numbers, the thermal conductivity of the porous solid is much larger than the convective cooling of the fluid medium. Hence, the solid phase approaches thermal equilibrium with the external surface of the cylinder. Increases in the Biot number and therefore strengthening the heat exchanges between the two phases of solid and fluid in the porous medium cause a drop in the temperature of the porous solid.

Figure 8b illustrates the radial distribution of dimensionless concentration for varying values of Reynolds number. This figure shows a similar behaviour to that observed in Fig. 4a, wherein dimensionless temperature drops by increases in Reynolds number. In both cases, increasing Reynolds number leads to reduction in the boundary layer thickness (thermal and concentration) and increases in the rate of transport (as shown in the following section).

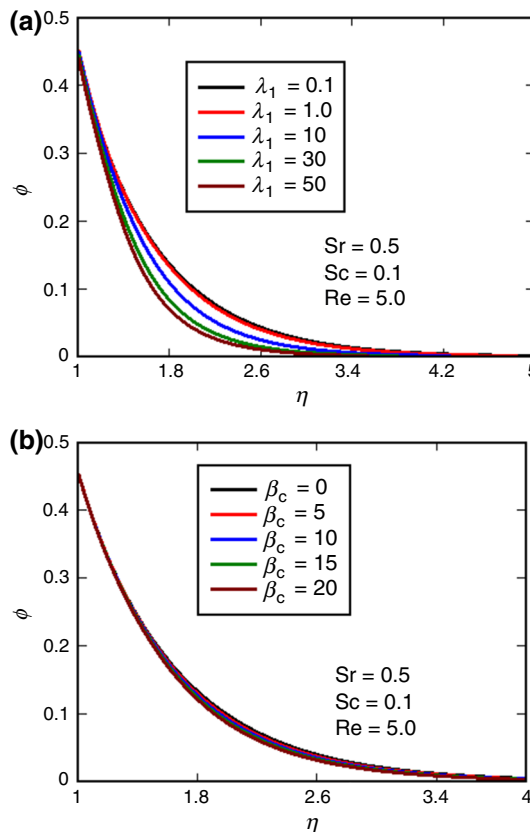


Fig. 9 Response of dimensionless concentration $\phi(\eta)$ to different values of **a** dimensionless mixed convection parameter, **b** nonlinear mixed convection parameter for concentration, $Df = 0.1$, $Bi = 0.1$, $Sr = 0.5$, $Re = 5.0$, $Sc = 0.1$, $\lambda = 10$, $\lambda_1 = 10$, $\beta_l = 0.1$, $\beta_c = 0.3$, $\beta_h = 0.1$

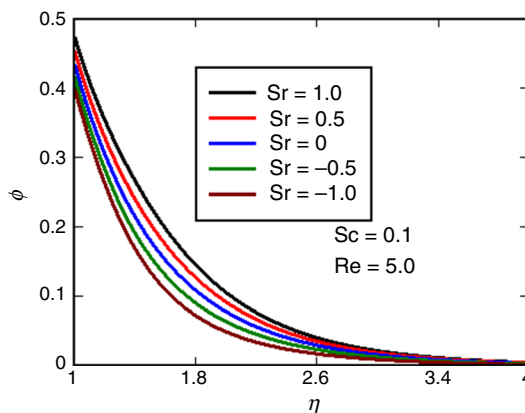


Fig. 10 Response of dimensionless concentration $\phi(\eta)$ to different values of Soret number $Df = 0.1$, $Bi = 0.1$, $Sr = 0.5$, $Re = 5.0$, $Sc = 0.1$, $\lambda = 10$, $\lambda_1 = 10$, $\beta_l = 0.1$, $\beta_c = 0.3$, $\beta_h = 0.1$

It should be noted that these results are further supported by the analogy between heat and mass transfer. Figure 9 shows the effects of mixed convection and nonlinear

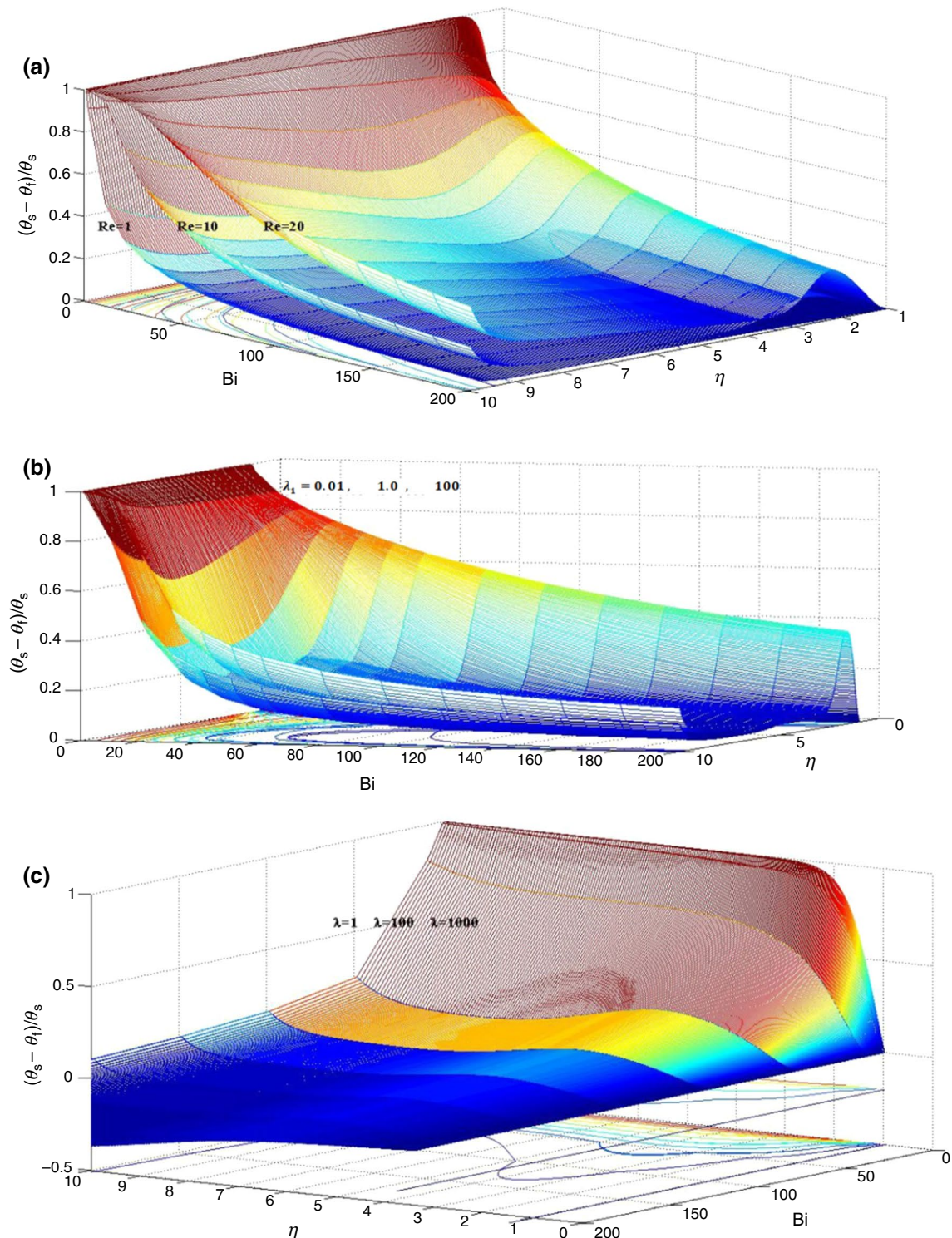


Fig. 11 Temperature difference between the fluid and porous solid phase, for different values of **a** Reynolds number, **b** dimensionless mixed convection parameter, **c** permeability parameter, $Df = 0.1$, $Bi = 0.1$, $Sr = 0.5$, $Re = 5.0$, $Sc = 0.1$, $\lambda = 10$, $\lambda_1 = 10$, $\beta_t = 0.1$, $\beta_c = 0.3$, $\beta_h = 0.1$

convection parameters upon the radial profiles of concentration. Higher values of mixed and nonlinear convection parameters (β_c) cause reductions in the thickness of the concentration boundary layer. Once again, these findings are in

qualitative agreement with those of temperature variation. Nonetheless, the effects of β_c on the thermal boundary layer appear to be stronger than those on the concentration boundary layer. Figure 10 shows that depending upon the sign of

Table 4 Impact of Prandtl and Schmidt number on the surface-averaged Sherwood, Nusselt and Bejan number, $Df = 1.0$, $Bi = 0.1$, $Sr = 0.5$, $Re = 5.0$, $Sc = 0.1$, $\lambda = 10$, $\lambda_1 = 1.0$, $\beta_t = 0.1$, $N^* = 1.0$, $\beta_c = 0.1$

Q_H	Nu_m	Sh_m	β_h	Nu_m	Sh_m	λ_1	Nu_m	Sh_m
0	1.469322	0.451961	0	1.735314	0.464441	0.01	1.719318	0.4641069
0.3	1.461031	0.452993	0.3	1.729541	0.464954	0.1	1.720283	0.4711376
0.5	1.457821	0.453015	0.5	1.719562	0.465453	1.0	1.729816	0.4774410
0.8	1.451811	0.453882	0.8	1.715213	0.466363	10	1.814899	0.4831836
1.0	1.443716	0.454287	1.0	1.711546	0.467474	50	2.074300	0.4958993

Table 5 Impact of Reynolds number and nonlinear convection parameters on the surface-averaged Sherwood, Nusselt and Bejan number, $Df = 1.0$, $Bi = 0.1$, $Sr = 0.5$, $Re = 10$, $Sc = 0.1$, $\lambda = 10$, $\lambda_1 = 10$, $\beta_t = 0.1$, $N^* = 50$, $\beta_c = 0.1$

Re	Nu_m	Sh_m	β_t	Nu_m	Sh_m	β_c	Nu_m	Sh_m
0.1	1.180332	0.4418018	0	1.644079	0.4580463	0	1.648651	0.4580465
1.0	1.667559	0.4563104	5.0	1.653584	0.4582736	5.0	1.844146	0.4645073
10	2.695047	0.5030617	10	1.662801	0.4584938	10	1.986441	0.4695192
50	3.951993	0.5532836	15	1.671753	0.4587073	15	2.100038	0.4736521
100	4.809386	0.5751724	20	1.680457	0.4589147	20	2.195405	0.4771866

Table 6 Impact of Dufour, Soret and Biot number on the surface-averaged Sherwood, Nusselt and Bejan number, $Df = 1.0$, $Bi = 0.1$, $Sr = 0.5$, $Re = 5.0$, $Sc = 0.1$, $\lambda = 10$, $\lambda_1 = 1.0$, $\beta_t = 10$, $N^* = 50$, $\beta_c = 0.1$

Df	Nu_m	Sh_m	Sr	Nu_m	Sh_m	Bi	Nu_m	Sh_m
0	2.016361	0.4696653	1.0	2.042746	0.4545306	0.1	1.986443	0.4695192
0.3	1.925952	0.4692409	0.5	1.986442	0.4695192	1.0	1.914141	0.4703451
0.5	1.864596	0.4689814	0	1.932564	0.4831708	10	1.755759	0.4723857
0.7	1.802364	0.4687411	-0.5	1.881332	0.4955133	100	1.664307	0.4744152
1.0	1.707362	0.4684174	-1.0	1.832952	0.5065943	200	1.652145	0.475334

Soret number, thermal diffusion can either enhance or suppress mass transfer process. For the set of parameters shown in Fig. 10, positive values of Soret number tend to increase the value of dimensionless concentration and reduce the rate of mass transfer, while the negative values of Soret number have the opposite effect.

Deviation from local thermal equilibrium and Nusselt and Sherwood numbers

Deviation from the state of local thermal equilibrium in porous media with chemical reactions has been already reported [18, 19, 50–54]. However, many numerical works still use local thermal equilibrium for reactive flows in porous media. Here, a systematic examination of the local thermal equilibrium of the system is put forward to identify the trends in deviation from local thermal equilibrium. Figure 11 shows surface plots of the temperature difference between the solid and fluid phase in the porous medium

against Biot number and radial coordinate and for different values of a few pertinent parameters. Biot number is known to be a key dimensionless parameter in evaluation of local thermal equilibrium and is therefore chosen as one of the main variables. In Fig. 11, the values of temperature difference close to one indicate strong tendency towards local thermal non-equilibrium. However, as the temperature difference approaches zero, local thermal equilibrium conditions are retained. As anticipated for all investigated cases, lower values of Biot number push the system towards local thermal non-equilibrium. This is because of the poor heat exchanges between the porous solid and fluid at smaller Biot numbers that allow for the development of a sizeable temperature difference between the two.

Figure 11 shows that for all values of Biot number, there is a finite temperature difference close to the surface of the solid. This region marks the thermal boundary layer, and as shown in Fig. 11a, it is thicker at lower values of Reynolds number. Outside this region and for larger radii, the

temperature difference increases slightly which is due to small changes in the temperature of porous solid. Figure 11a further shows that increasing Reynolds number intensifies the deviation from local thermal equilibrium, while Fig. 11b, c indicates that increases in mixed convection and permeability parameters have the same effect.

The values of the surface-averaged Nusselt and Sherwood number calculated for several different parameters are shown in Tables 4–6. Values of surface-averaged Nusselt and Sherwood number vary slightly by changes in the nonlinear heat generations (see Table 4). However, they are quite sensitive to changes in permeability parameter. Also, as discussed earlier, increases in Reynolds number and nonlinear convection parameters (β_c and β_T) magnify the values of Nusselt and Sherwood number (see Table 5). The extent of these magnifications is quite strong for Reynolds number and β_c but rather insignificant for β_T . Finally, as shown in Table 6, increases in Biot and Dufour number reduce Nusselt and Sherwood number. Nonetheless, depending upon its sign, Soret effect can either increase or reduce Nusselt number [55–58].

Conclusions

Combined transport of heat and mass through mixed convection set by the impingement of a flow over a vertical cylinder embedded in a porous medium was considered. The surface of cylinder was coated with a catalytic material leading to the occurrence of a heterogenous chemical reaction. Nonlinear convection of heat and mass and nonlinear heat generations were considered, and the formulation of the problem included Soret and Dufour effects. The nonlinear governing equations were reduced to a system of ordinary differential equations by using similarity variables. A finite difference method was then used to solve the coupled, nonlinear ordinary differential equations. The findings of this study can be summarised as follows.

- Increasing Reynolds number results in the reduction in the thicknesses of thermal and concentration boundary layers. Consequently, it enhances the value of Nusselt and Sherwood number.
- Higher values of nonlinear mixed convection parameters make the boundary layers thinner and therefore enhance the rate of heat and mass transfer.
- The effects of nonlinear mixed convection parameter for concentration appeared to be stronger than those of thermal mixed convection.
- Soret and Dufour numbers were found to be influential on the value of Sherwood and Nusselt number. Nonetheless, their effects are either comparable or less than the influences of nonlinear mixed convection.

- Deviation of the porous system from local thermal equilibrium was systematically examined. This showed that increases in Reynolds and mixed convection parameters push the system towards local thermal non-equilibrium.

The current study clearly demonstrated the potential significance of nonlinear mixed convection. Future studies will focus on exploring the complex interaction between momentum transfer and nonlinear convection of heat and mass.

Acknowledgements This work was supported by the Natural Science Foundation of the Higher Education Institutions of Jiangsu Province (17KJA530001) and Foundation of Huaian Municipal Science and Technology Bureau (HAA201734). Dr. Hong thanks the support of Six Talent Peaks Project of Jiangsu Province (2018-XNY-004).

References

1. Wu Q, Weinbaum S, Andreopoulos Y. Stagnation-point flows in a porous medium. *Chem Eng Sci*. 2005;60(1):123–34.
2. Ishak A, Nazar R, Arifin NM, Pop I. Dual solutions in mixed convection flow near a stagnation point on a vertical porous plate. *Int J Therm Sci*. 2008;47(4):417–22.
3. Kokubun MA, Fachini FF. An analytical approach for a Hiemenz flow in a porous medium with heat exchange. *Int J Heat Mass Transf*. 2011;54(15):3613–21.
4. Nazari M, Shakerinejad E, Nazari M, Rees DAS. Natural convection induced by a heated vertical plate embedded in a porous medium with transpiration: local thermal non-equilibrium similarity solutions. *Transp Porous Media*. 2013;98(1):223–38.
5. Feng SS, Kuang JJ, Wen T, Lu TJ, Ichimiya K. An experimental and numerical study of finned metal foam heat sinks under impinging air jet cooling. *Int J Heat Mass Transf*. 2014;77:1063–74.
6. Mabood F, Khan WA, Ismail AM. MHD stagnation point flow and heat transfer impinging on stretching sheet with chemical reaction and transpiration. *Chem Eng J*. 2015;273:430–7.
7. Postelnicu A. Influence of chemical reaction on heat and mass transfer by natural convection from vertical surfaces in porous media considering Soret and Dufour effects. *Heat Mass Transf*. 2007;43(6):595–602.
8. Postelnicu A. Heat and mass transfer by natural convection at a stagnation point in a porous medium considering Soret and Dufour effects. *Heat Mass Transf*. 2010;46(8–9):831–40.
9. Postelnicu A. Influence of a magnetic field on heat and mass transfer by natural convection from vertical surfaces in porous media considering Soret and Dufour effects. *Int J Heat Mass Transf*. 2004;47(6–7):1467–72.
10. Tsai R, Huang JS. Heat and mass transfer for Soret and Dufour's effects on Hiemenz flow through porous medium onto a stretching surface. *Int J Heat Mass Transf*. 2009;52(9–10):2399–406.
11. Al-Sumaily GF, Hussien HM, Thompson MC. Validation of thermal equilibrium assumption in free convection flow over a cylinder embedded in a packed bed. *Int Commun Heat Mass Transf*. 2014;58:184–92.
12. Alizadeh R, Rahimi AB, Karimi N, Alizadeh A. On the hydrodynamics and heat convection of an impinging external flow upon a cylinder with transpiration and embedded in a porous medium. *Transp Porous Media*. 2017;120(3):579–604. <https://doi.org/10.1007/s11242-017-0942-9>.
13. Alizadeh R, Karimi N, Arjmandzadeh R, Mehdizadeh A. Mixed convection and thermodynamic irreversibilities in MHD nanofluid

- stagnation-point flows over a cylinder embedded in porous media. *J Therm Anal Calorim.* 2018;135(1):489–506. <https://doi.org/10.1007/s10973-018-7071-8>.
14. Alizadeh R, Karimi N, Mehdizadeh A, Nourbakhsh A. Analysis of transport from cylindrical surfaces subject to catalytic reactions and non-uniform impinging flows in porous media—a non-equilibrium thermodynamics approach. *J Therm Anal Calorim.* 2019. <https://doi.org/10.1007/s10973-019-08120-z>.
 15. Afify AA. Effects of temperature-dependent viscosity with Soret and Dufour numbers on non-Darcy MHD free convective heat and mass transfer past a vertical surface embedded in a porous medium. *Transp Porous Media.* 2007;66(3):391–401.
 16. Chamkha AJ, Ben-Nakhi A. MHD mixed convection–radiation interaction along a permeable surface immersed in a porous medium in the presence of Soret and Dufour’s effects. *Heat Mass Transf.* 2008;44(7):845.
 17. Pal D, Chatterjee S. Soret and Dufour effects on MHD convective heat and mass transfer of a power-law fluid over an inclined plate with variable thermal conductivity in a porous medium. *Appl Math Comput.* 2013;219(14):7556–74.
 18. Karimi N, Agbo D, Talat Khan A, Younger PL. On the effects of exothermicity and endothermicity upon the temperature fields in a partially-filled porous channel. *Int J Therm Sci.* 2015;96:128–48. <https://doi.org/10.1016/j.ijthermalsci.2015.05.002>.
 19. Torabi M, Karimi N, Zhang K. Heat transfer and second law analyses of forced convection in a channel partially filled by porous media and featuring internal heat sources. *Energy.* 2015;93:106–27. <https://doi.org/10.1016/j.energy.2015.09.010>.
 20. Jeng TM, Tzeng SC. Numerical study of confined slot jet impinging on porous metallic foam heat sink. *Int J Heat Mass Transf.* 2005;48(23–24):4685–94.
 21. Jeng TM, Tzeng SC. Experimental study of forced convection in metallic porous block subject to a confined slot jet. *Int J Therm Sci.* 2007;46(12):1242–50.
 22. Wong KC, Saeid NH. Numerical study of mixed convection on jet impingement cooling in a horizontal porous layer under local thermal non-equilibrium conditions. *Int J Therm Sci.* 2009;48(5):860–70.
 23. Wong KC. Thermal analysis of a metal foam subject to jet impingement. *Int Commun Heat Mass Transf.* 2012;39(7):960–5.
 24. Hwang ML, Yang YT. Numerical simulation of turbulent fluid flow and heat transfer characteristics in metallic porous block subjected to a confined slot jet. *Int J Therm Sci.* 2012;55:31–9.
 25. Marafie A, Khanafer K, Al-Azmi B, Vafai K. Non-Darcian effects on the mixed convection heat transfer in a metallic porous block with a confined slot jet. *Numer Heat Transf Part A.* 2008;54(7):665–85.
 26. Harris SD, Ingham DB, Pop I. Mixed convection boundary-layer flow near the stagnation point on a vertical surface in a porous medium: Brinkman model with slip. *Trans Porous Media.* 2009;77(2):267–85.
 27. Sivasamy A, Selladurai V, Kanna PR. Mixed convection on jet impingement cooling of a constant heat flux horizontal porous layer. *Int J Therm Sci.* 2010;49(7):1238–46.
 28. Buonomo B, Lauriat G, Manca O, Nardini S. Numerical investigation on laminar slot-jet impinging in a confined porous medium in local thermal non-equilibrium. *Int J Heat Mass Transf.* 2016;98:484–92.
 29. Makinde OD. Heat and mass transfer by MHD mixed convection stagnation point flow toward a vertical plate embedded in a highly porous medium with radiation and internal heat generation. *Mechanica.* 2012;47(5):1173–84.
 30. Rosca NC, Pop I. Mixed convection stagnation point flow past a vertical flat plate with a second order slip: heat flux case. *Int J Heat Mass Transf.* 2013;65:102–9.
 31. Hayat T, Abbas Z, Pop I, Asghar S. Effects of radiation and magnetic field on the mixed convection stagnation-point flow over a vertical stretching sheet in a porous medium. *Int J Heat Mass Transf.* 2010;53(1):466–74.
 32. Qayyum S, Hayat T, Alsaedi A, Ahmad B. Magnetohydrodynamic (MHD) nonlinear convective flow of Jeffrey nanofluid over a nonlinear stretching surface with variable thickness and chemical reaction. *Int J Mech Sci.* 2017;134:306–14.
 33. Qayyum S, Hayat T, Shehzad SA, Alsaedi A. Nonlinear convective flow of Powell–Eyring magneto nanofluid with Newtonian heating. *Results Phys.* 2017;7:2933–40.
 34. Hayat T, Qayyum S, Alsaedi A, Ahmad B. Magnetohydrodynamic (MHD) nonlinear convective flow of Walters-B nanofluid over a nonlinear stretching sheet with variable thickness. *Int J Heat Mass Transf.* 2017;110:506–14.
 35. Hayat T, Qayyum S, Alsaedi A, Ahmad B. Nonlinear convective flow with variable thermal conductivity and Cattaneo–Christov heat flux. *Neural Comput Appl.* 2019;31(1):295–305.
 36. Khan MI, Qayyum S, Hayat T, Khan MI, Alsaedi A, Khan TA. Entropy generation in radiative motion of tangent hyperbolic nanofluid in presence of activation energy and nonlinear mixed convection. *Phys Lett A.* 2018;382(31):2017–26.
 37. Hunt G, Karimi N, Torabi M. Two-dimensional analytical investigation of coupled heat and mass transfer and entropy generation in a porous, catalytic microreactor. *Int J Heat Mass Transf.* 2018;119:372–91.
 38. Hunt G, Torabi M, Govone L, Karimi N, Mehdizadeh A. Two-dimensional heat and mass transfer and thermodynamic analyses of porous microreactors with Soret and thermal radiation effects—an analytical approach. *Chem Eng Process.* 2018;126:190–205.
 39. Govone L, Torabi M, Wang L, Karimi N. Effects of nanofluid and radiative heat transfer on the double-diffusive forced convection in microreactors. *J Therm Anal Calorim.* 2019;135(1):45–59.
 40. Atkins P. *Physical chemistry: thermodynamics, structure, and change.* London: Macmillan Higher Education; 2014.
 41. Cunnning GM, Davis AMJ, Weidman PD. Radial stagnation flow on a rotating circular cylinder with uniform transpiration. *J Eng Math.* 1998;33(2):113–28.
 42. Alizadeh R, Rahimi AB, Arjmandzadeh R, Najafi M, Alizadeh A. Unaxisymmetric stagnation-point flow and heat transfer of a viscous fluid with variable viscosity on a cylinder in constant heat flux. *Alex Eng J.* 2016;55(2):1271–83.
 43. Gomari S, Alizadeh R, Alizadeh A, Karimi N. Generation of entropy during forced convection of heat in nanofluid stagnation-point flow over a cylinder embedded in porous media. *Numer Heat Transf Part A.* 2019;75(10):647–73.
 44. Alizadeh R, Karimi N, Mehdizadeh A, Nourbakhsh A. Effect of radiation and magnetic field on mixed convection stagnation-point flow over a cylinder in a porous medium under local thermal non-equilibrium. *J Therm Anal Calorim.* 2019. <https://doi.org/10.1007/s10973-019-08415-1>.
 45. Thomas JW. *Numerical partial differential equations: finite difference methods, vol. 22.* Berlin: Springer; 2013.
 46. Wang CY. Axisymmetric stagnation flow on a cylinder. *Q Appl Math.* 1974;32(2):207–13.
 47. Gorla RSR. Heat transfer in an axisymmetric stagnation flow on a cylinder. *Appl Sci Res.* 1976;32(5):541–53.
 48. Incropera FP, Lavine AS, Bergman TL, DeWitt DP. *Fundamentals of heat and mass transfer.* New York: Wiley; 2007.
 49. Torabi M, Zhang K, Karimi N, Peterson GP. Entropy generation in thermal systems with solid structures—a concise review. *Int J Heat Mass Transf.* 2016;97:917–31.
 50. Asadi A, Kadijani ON, Doranehgard MH, Bozorg MV, Xiong Q, Shadloo MS, Li LK. Numerical study on the application of biodiesel and bioethanol in a multiple injection diesel engine. *Renew Energy.* 2019. <https://doi.org/10.1016/j.renene.2019.11.088>.

51. Saffarian MR, Moravej M, Doranehgard MH. Heat transfer enhancement in a flat plate solar collector with different flow path shapes using nanofluid. *Renew Energy*. 2020;146:2316–29.
52. Bozorg MV, Doranehgard MH, Hong K, Xiong Q. CFD study of heat transfer and fluid flow in a parabolic trough solar receiver with internal annular porous structure and synthetic oil–Al₂O₃ nanofluid. *Renew Energy*. 2020;145:2598–614.
53. Gholamalipour P, Siavashi M, Doranehgard MH. Eccentricity effects of heat source inside a porous annulus on the natural convection heat transfer and entropy generation of Cu–water nanofluid. *Int Commun Heat Mass Transf*. 2019;109:104367.
54. Athar K, Doranehgard MH, Eghbali S, Dehghanpour H. Measuring diffusion coefficients of gaseous propane in heavy oil at elevated temperatures. *J Therm Anal Calorim*. 2019. <https://doi.org/10.1007/s10973-019-08768-7>.
55. Xiong Q, Bozorg MV, Doranehgard MH, Hong K, Lorenzini G. A CFD investigation of the effect of non-Newtonian behavior of Cu–water nanofluids on their heat transfer and flow friction characteristics. *J Therm Anal Calorim*. 2019. <https://doi.org/10.1007/s10973-019-08757-w>.
56. Siavashi M, Karimi K, Xiong Q, Doranehgard MH. Numerical analysis of mixed convection of two-phase non-Newtonian nanofluid flow inside a partially porous square enclosure with a rotating cylinder. *J Therm Anal Calorim*. 2019;137(1):267–87.
57. Mesbah M, Vatani A, Siavashi M, Doranehgard MH. Parallel processing of numerical simulation of two-phase flow in fractured reservoirs considering the effect of natural flow barriers using the streamline simulation method. *Int J Heat Mass Transf*. 2019;131:574–83.
58. Guthrie DGP, Torabi M, Karimi N. Combined heat and mass transfer analyses in catalytic microreactors partially filled with porous material—the influences of nanofluid and different porous-fluid interface models. *Int J Therm Sci*. 2019;140:96–113.

Publisher's Note Springer Nature remains neutral with regard to jurisdictional claims in published maps and institutional affiliations.